Bismuth-Based Metal-Organic Frameworks for Water Vapor Capture and Energy Storage

Jianxin Ma, Chen Wang, Qianqian Liu, Xinyu Chen, Bo Li, Zhong-Min Su,* Ya-Qian Lan,* and Hong-Ying Zang*

Transforming water vapor into electricity is a critical method for advancing renewable energy supply and alleviating the global energy crisis. However, conventional materials typically struggle to achieve a balance between energy storage and humidity harvesting, making the integration of humidity detection with energy storage technology an emerging challenge. To address this challenge, a novel material design strategy is explored aimed at combining humidity harvesting capabilities with energy storage. Two novel hygroscopic Bi-based metal-organic frameworks $[Bi_2(HABTC)(ABTC)_{0.5}\cdot 4H_2O]$ (MOF 1) and $[Bi_4(ABTC)_3(DMF)_2]\cdot DMF$ (MOF 2) are grown in situ on carbon paper electrodes, followed by further modification with polyaniline (PANI). This approach enhances the hygroscopicity of materials, thereby improving electrochemical performance, doubling the energy density compared to traditional coating methods. The integration of humidity-sensitive polyoxometalates (POMs) electrolytes create a synergistic interaction between the electrode and the electrolyte, enabling effective moisture energy harvesting. At 90% relative humidity (RH) and 70 °C, the constructed solid-state capacitor demonstrates a high energy density of 40.40 Wh kg^{-1} at 499.82 W kg^{-1}. This research not only confirms the feasibility of water vapor energy harvesting but also paves an innovative pathway in the field of humidity energy conversion, highlighting its significant potential for future practical applications.

1. Introduction

The ubiquitous presence of water vapor in the atmosphere has spurred interest in the development of energy-harvesting technologies based on water vapor utilization.[1–4] The concept of harnessing energy from ambient water vapor to create renewable energy is intriguing, suggesting that the water vapor present in the atmosphere could potentially be transformed into a practical and viable renewable energy source.[5–7] This idea has spurred the search for innovative methods of capturing humidity and storing energy. In light of this, the concept of humidity energy storage has gained traction as a novel environmental energy conversion method, offering a promising approach to directly utilize water vapor in the air.[8–10] Consequently, the integration of water vapor utilization with energy devices has emerged as a potent strategy for harnessing this plentiful resource effectively.[11,12]

Supercapacitors (SCs), as an advanced energy storage technology, are designed for rapid charging and discharging, high-power output, and are widely used in portable electronic devices,[13–18] renewable energy storage systems, and smart grids.[19–22] Building on this utility, supercapacitors further advance the cutting edge by ingeniously integrating water vapor capture with energy storage. This fusion of technologies effectively converts ambient humidity into electrical energy, creating a novel integrated system that combines

J. Ma
School of Materials Science and Engineering
Changchun University of Science and Technology
Changchun 130022, P. R. China
J. Ma, Z.-M. Su
School of Chemistry and Environmental Engineering
Changchun University of Science and Technology
Changchun 130022, P. R. China
E-mail: zmsu@nenu.edu.cn
C. Wang, Z.-M. Su
State Key Laboratory of Supramolecular Structure and Materials
Institute of Theoretical Chemistry
College of Chemistry
Jilin University
Changchun 130021, P. R. China

Q. Liu, X. Chen, B. Li, H.-Y. Zang
Key Laboratory of Polyoxometalate and Reticular Material Chemistry of Ministry of Education at Universities of Jilin Province
Faculty of Chemistry Northeast Normal University
Changchun 130024, P. R. China
E-mail: zanghy100@nenu.edu.cn
Y.-Q. Lan
Guangdong Provincial Key Laboratory of Carbon Dioxide Resource Utilization
School of Chemistry South China Normal University
Guangzhou 510006, P. R. China
E-mail: yqlan@m.scnu.edu.cn

ADVANCED
SCIENCE NEWS

www.advancedsciencenews.com

ADVANCED
FUNCTIONAL
MATERIALS

www.afm-journal.de

energy harvesting and storage, achieving seamless and efficient energy conversion and storage. However, the pivotal factor in realizing this advancement hinges on the innovation of superior electrode materials and advanced electrolytes, as well as the synergy between them.[23,24] MOFs have been selected as electrode materials due to their high specific surface area, tunable structures, and excellent moisture absorption properties, which are essential for enhancing electrode performance.[25–29] To avoid the use of ineffective adhesives and ensure strong adhesion between the MOFs and the carbon paper (CP), we employed an in situ growth method. This approach directly enhances the electrochemical performance and stability of the supercapacitors.[30–32] Furthermore, to augment the material's performance, conductive polyaniline was combined with the MOF-carbon paper,[33–35] facilitating the formation of a dense and porous structure that increases the material's adsorption capacity for water vapor.[36–38]

Polyoxometalates (POMs) exhibit high ionic conductivity and electron-sponge properties, making them ideal candidates in supercapacitors.[39,40] The proton-coupled electron transfer characteristic of POMs is crucial for supporting this dual functionality and directly boosting the efficiency of energy storage in supercapacitors.[41] Acting as a bridge between humidity and energy conversion, the proton conductivity of POMs is closely related to their response to humidity, while their electron storage capacity is tightly linked to the functionality of supercapacitors.[42,43] Therefore, using POMs as a medium for simultaneous humidity sensing and energy storage not only provides an efficient conversion platform but also establishes an innovative connection between humidity energy harvesting and storage.

Based on these findings, we developed novel solid-state supercapacitors that harness humidity to boost electrical energy, using moisture-absorbent carbon paper as electrodes and humidity-sensitive POMs as electrolytes. We employed an in situ growth technique to immobilize two humidity-absorbent MOFs based on bismuth and H_4ABTC onto the carbon paper and modified them with conductive polyaniline to enhance ion transport, charge transfer, and moisture absorption. The electrode-electrolyte interface was stabilized by electrostatic interactions, with partial infiltration of the POM-gel electrolyte into the electrodes. This synergistic effect increased the pseudocapacitance and enhanced the overall performance, resulting in the constructed solid-state supercapacitor achieving a high energy density of 40.40 Wh kg^{-1}. After 1000 charge–discharge cycles, the supercapacitor retained 92.17% of its initial capacitance and successfully powered a micro-LED, demonstrating its practicality. This research not only provides a new direction for the design of environmentally adaptive supercapacitors but also lays a solid scientific foundation for the development of energy storage technologies.
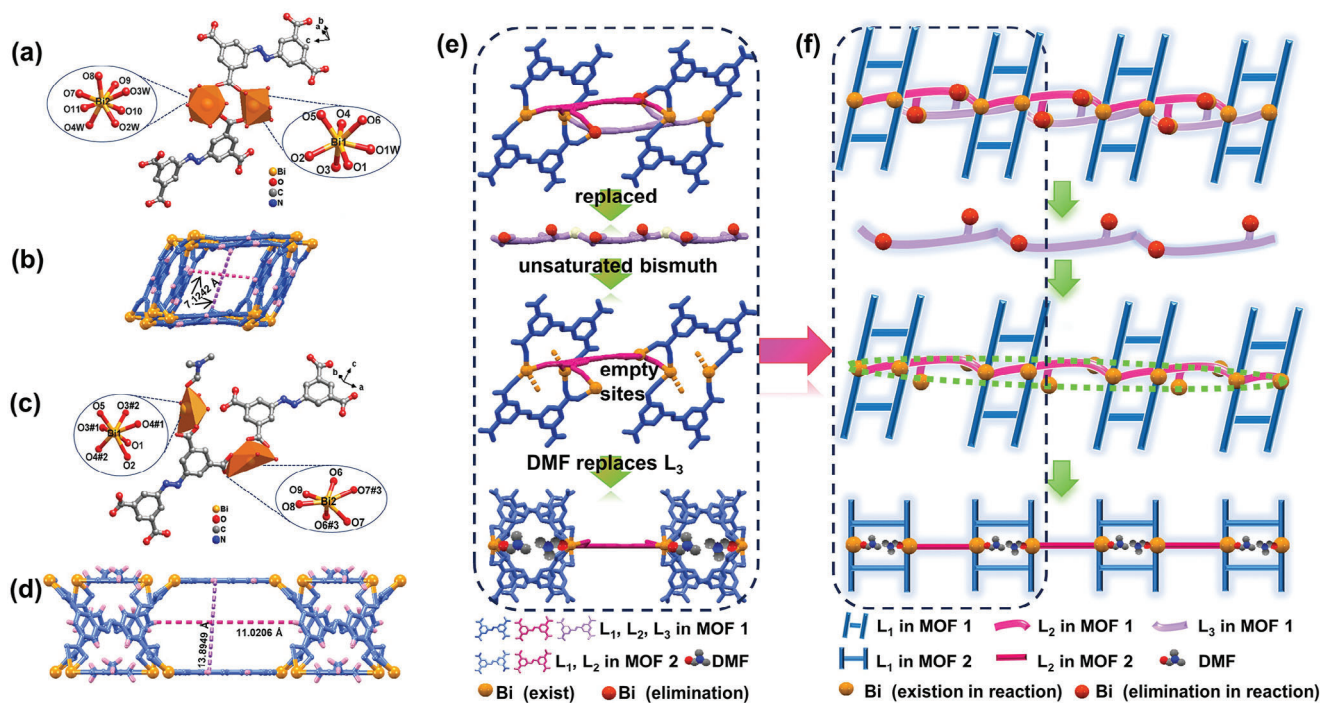
2. Results and Discussion

Single crystal X-ray crystallographic analysis revealed that MOF **1** and MOF **2** crystallize in the Triclinic space group $P\bar{1}$ and Monoclinic space group $C12/m1$. The crystal data collection, selected bond lengths, and angles of MOF **1** and MOF **2** are summarized in Tables S1–S3 (Supporting Information), respectively. We discuss the structures of MOF **1** and MOF **2** in detail. MOF **1** and MOF **2** are structurally similar, but differ in the coordination

modes of Bi ions, the most immediate difference being that MOF **2** has solvent DMF coordination. In MOF **1**, Bi ions are seven- and eight-coordinated (**Figure 1a**), and in MOF **2**, Bi ions are six- and seven-coordinated (Figure 1c). The coordination environment of MOF **1** is constructed with two central Bi ions, eleven O atoms from seven H_4ABTC, and O atoms from coordinated water. The distances of Bi—O bonds range from 2.276(7) to 2.493(7) Å. In MOF **2**, two Bi centers are coordinated by twelve O atoms from five H_4ABTC and one O atom from DMF with the typical Bi—O bond lengths (Bi—O, 2.240(12)–2.722(10) Å).

In MOF **1** and MOF **2**, H_4ABTC ligands are classified as long-edge L1 and short-edge L2 and L3, creating unique coordination around Bi chains. L1 is crucial for framework stability. In MOF **1**, symmetric L2 and L3 ligands coordinate with Bi atoms (Figure 1e), except for water, but their flexibility reduces porosity and hinders material performance studies. To rectify this, we linked DMF to the MOF structure, by increasing the DMF concentration in the solvent to replace ligands and enhance porosity. This approach was effective in MOF **2**, in which DMF replaced L3, allowing L1 to stand upright for stability (Figure 1f). MOF **2** (Figure 1d) represents a deformation of MOF **1** (Figure 1b) with larger pores and improved stability. The 3D frameworks of MOF **1** (Figure S1, Supporting Information) and MOF **2** (Figure S2, Supporting Information) are characterized by a binodal network topology, with the coupling groups of the H_4ABTC ligands serving as connection points. Initially, a 2D layered architecture is created, which is then expanded into a 3D networked structure through these interconnect nodes. Through optimization of the interaction between Bi^{3+} and DMF, an ideal framework is provided by MOF **2** with increased storage and active sites for enhanced electrode material performance.[44,45]

Powder X-ray diffraction (PXRD) patterns of the as-synthesized and in situ samples demonstrated that they possess good crystallinity and phase purity (Figure S3, Supporting Information). Figure S4 (Supporting Information) shows the FT-IR spectra of MOF **1**, in situ-MOF **1**, MOF **2**, and in situ-MOF **2**. The absorption peak corresponding to the $-COO^-$ asymmetric stretching vibration ($\nu_{as}(COO^-)$) was observed near 1600 cm^{-1}. Simultaneously, the absorption peak of $-COO^-$ symmetric stretching vibration ($\nu_s(COO^-)$) was observed near 1350 cm^{-1}, indicating the coordination of the carboxyl group with Bi^{3+}.[46] A stretching vibration at 3500 cm^{-1} can be ascribed to the $\nu(O-H)$ vibration.[47] The bands observed at 987 and 916 cm^{-1} indicated the different stretching modes of the $\nu(C-N)$ bond.[48] The TGA measurements of MOF **1** and MOF **2** were conducted under N_2 atmosphere from 30 to 700 °C (Figure S5, Supporting Information). MOF **1** exhibited a gradual weight loss in the first stage from 30 to 170 °C (7.28%), which is likely due to the removal of four H_2O molecules. In contrast, MOF **2** showed a slow weight loss in the first stage from 30 to 120 °C (7.10%), which is attributed to the evaporation of two DMF molecules. The second weight loss from 150 to 190 °C (3.55%) corresponds to the release of one additional DMF molecule. The water vapor adsorption capacity of MOF **1** and MOF **2** was evaluated (Figure 3a). The maximum water vapor adsorption capacities of MOF **1** and MOF **2** at 30 °C are 129.6 and 198.7 mg g^{-1}, respectively. X-ray photoelectron spectroscopy (XPS) tests were further performed to analyze the chemical
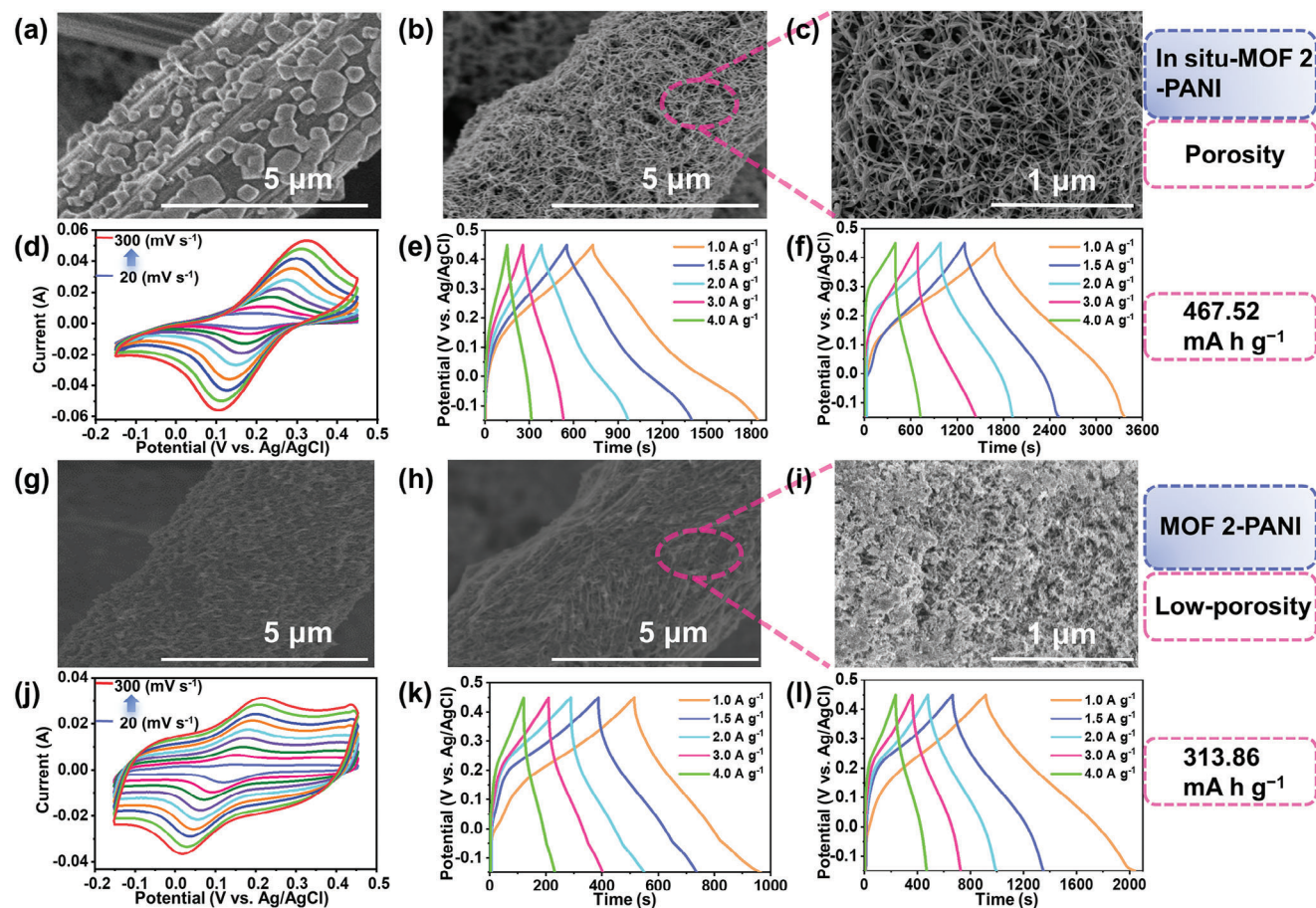
ADVANCED
SCIENCE NEWS

www.advancedsciencenews.com

ADVANCED
FUNCTIONAL
MATERIALS

www.afm-journal.de

Figure 1. The coordination environment of a) MOF **1** and c) MOF **2**. The pore size of b) MOF **1** and d) MOF **2**. Dotted lines highlight the H···H distances. Color codes: Bi, yellow; H, pink. Both the ligands and water are depicted in shades of blue for clarity. e) The illustration of the structural transformation from MOF **1** to MOF **2**. f) Concise depiction of the transformation between MOF **1** and MOF **2** structures.

composition of MOF **1** and MOF **2**. Figure S6 (Supporting Information) displays the full XPS spectra of MOF **1** and MOF **2**, and Figure S7 (Supporting Information) confirms the presence of Bi, O, N, and C elements in the prepared MOFs. Collectively, these results confirm the successful preparation of MOF **1** and MOF **2**, which are suitable for subsequent performance evaluations.

MOFs are renowned for their superior qualities in supercapacitor electrodes but pose integration challenges with carbon paper. In situ growth is a standout technique for electrode preparation, which allows in situ grown MOF on carbon paper. This enhances electrode conductivity and stability. Thus, we utilized an in situ growth technique to fabricate MOFs directly on carbon paper, yielding electrodes with superior conductivity, named in situ-MOF **1**-CP and in situ-MOF **2**-CP. The successful in situ growth of MOFs on the carbon paper was substantiated by PXRD (Figure S3, Supporting Information) and IR (Figure S4, Supporting Information) analysis. Furthermore, scanning electron microscopy (SEM) was employed to examine the morphology (Figure S8e, Supporting Information; **Figure 2a**), revealing a uniform and dense growth of MOFs on the carbon paper electrode surface. The electrochemical performance of the in situ grown MOF electrodes was evaluated using cyclic voltammetry (CV) and galvanostatic charge–discharge (GCD) methods, within a three-electrode system in a 0.5 M H_2SO_4 solution. The CV curves of in situ-MOF **1**-CP and in situ-MOF **2**-CP at different scan rates (20 to 300 mV s^{-1}) are shown in Figure S9a (Supporting Information) and Figure 2d. Notably, the CV curve of in situ-MOF **2** was broader than that of in situ-MOF **1** (Figure S10, Supporting Information), suggesting a higher utilization of redox-active groups.

The GCD measurements show specific capacities of 157.32 mA h g^{-1} for in situ-MOF **1** (Figure S9b, Supporting Information) and 309.89 mA h g^{-1} for in situ-MOF **2**-CP (Figure 2e) at 1 A g^{-1}. To enhance the conductivity of the electrode materials, the active substance PANI was applied to the electrode surface via electrodeposition, creating in situ-MOF **n**@PANI electrode (**n** = **1** or **2**). SEM images reveal the microstructural changes after the deposition of polyaniline, showing that the in situ-MOF **2**@PANI fibers (Figure 2b,c) had more pronounced pores than those of in situ-MOF **1**@PANI fibers (Figure S8f, Supporting Information). This more open pore structure facilitates the entry of electrolyte ions, improving their utilization rate. We investigated the effect of PANI electrodeposition on the capacitance performance. The specific capacity varies with the change in current density, with a noticeable reduction in capacitance occurring as the current density intensifies. At lower current densities, the electrolyte ions may fully penetrate the internal active sites, thereby increasing the electrode capacitance. Conversely, higher current densities result in a sharp decrease in capacitance. At a current density of 1 A g^{-1}, the specific capacity of the in situ-MOF **1**@PANI (Figure S9c, Supporting Information) was 328.83 mA h g^{-1}. In contrast, the in situ-MOF **2**@PANI (Figure 2f) demonstrates a higher specific capacity of 467.52 mA h g^{-1}. By applying a polyaniline coating to in situ grown MOF electrodes, a substantial improvement in electrode performance has been achieved. The pore size of the MOF aids in the formation of a porous structure within the polyaniline fibers, enhancing water adsorption capacity (Figure S11, Supporting Information) and allowing more water molecules to infiltrate the pores. The deposition of polyaniline increases the specific surface area of the electrode and introduces additional

**ADVANCED
SCIENCE NEWS**

www.advancedsciencenews.com

**ADVANCED
FUNCTIONAL
MATERIALS**

www.afm-journal.de

Figure 2. a–c,g–i) SEM images of in situ-MOF **2**-CP and MOF **2**-CP. d,j) The CV curves for in situ-MOF **2**-CP and MOF **2**-CP. e,k) The GCD curves for in situ-MOF **2**-CP and MOF **2**-CP. f,l) The GCD curves of in situ-MOF **2**@PANI and MOF **2**@PANI.
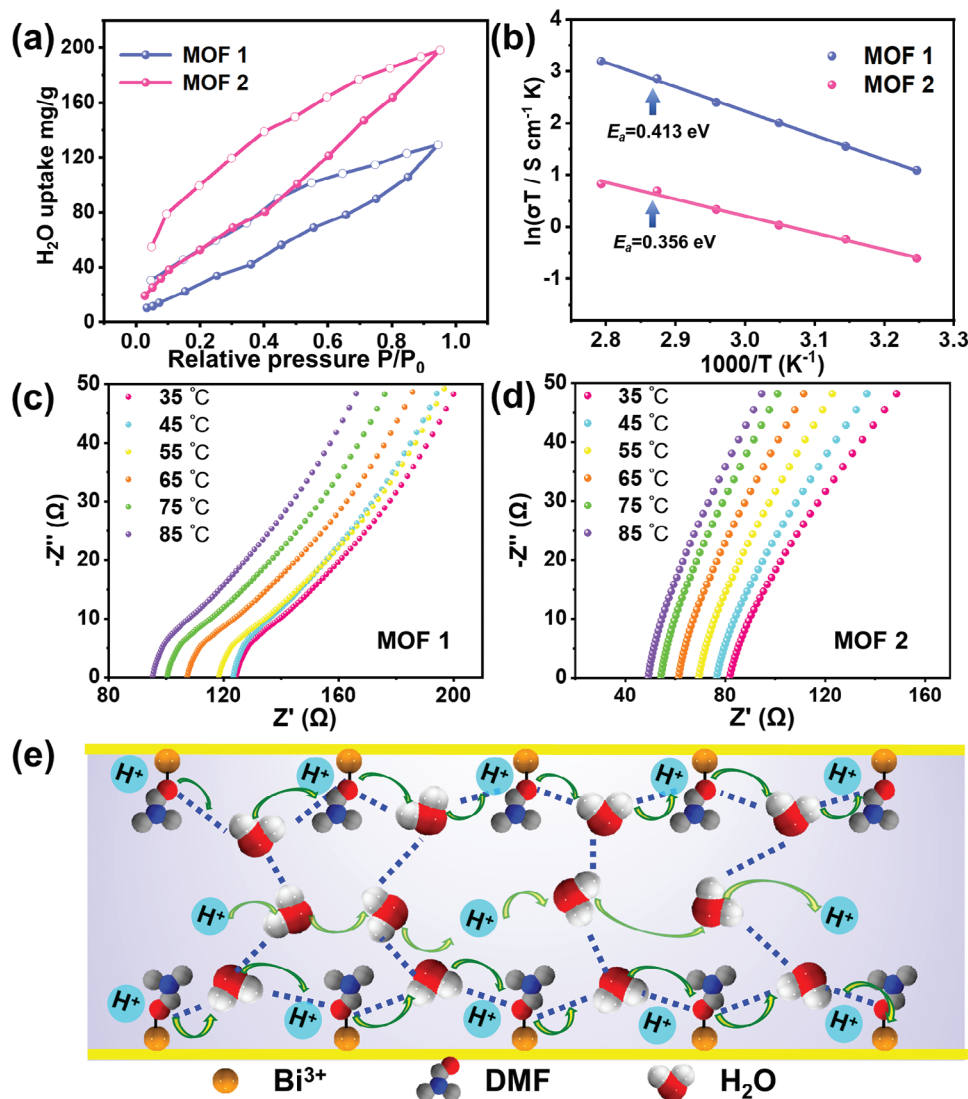
active sites for charge storage, which in turn enhances the electrode's electrical conductivity and capacitance. It is this structural enhancement that underpins the superior electrode performance of the polyaniline-coated in situ-MOF **2**-CP.

To ascertain whether the in situ growth electrode method surpasses the conventional coating method, we prepared electrodes using the slurry coating technique and conducted a comprehensive comparative analysis with the in situ grown MOF electrodes. The SEM images of the coated electrodes for MOF **1** (Figure S8 h, Supporting Information) and MOF **2** (Figure 2g), as well as their polyaniline-coated counterparts (Figure S8i (Supporting Information) for MOF **1**, Figure 2h,i for MOF **2**), indicate that the surfaces of the coated electrodes are dense, uneven, and robust, with the polyaniline layer failing to form a loose porous structure. However, the polyaniline fibers of MOF **2** exhibit larger pore sizes compared to MOF **1**, which aligns with our previous conclusion that the pore size can regulate the porosity of polyaniline fibers. Furthermore, the CV curves of MOF **1** and MOF **2**, as depicted in Figure S9d (Supporting Information) and Figure 2j, both showed good reversible redox peaks, indicating satisfactory electrochemical activity. At the current density of 1 A g^{-1}, the GCD curves of MOF **1** (Figure S9e, Supporting Information), MOF **2** (Figure 2k), MOF **1**@PANI (Figure S9f, Supporting Information), and MOF **2**@PANI (Figure 2l) demonstrate specific

capacities of 31.38, 125.85, 172.54, 313.86 mA h g^{-1}, respectively, which is significantly lower than that of the in situ grown MOF electrodes. As shown in the EIS spectrum of Figure S13 (Supporting Information), the resistance of MOF **2**-CP is lower than that of MOF **1**-CP, indicating that MOF **2**-CP has faster electron transfer than MOF **1**-CP.

These results indicate that the in situ-MOF electrodes exhibit excellent electrochemical performance, surpassing the majority of existing MOF-based solid-state supercapacitors (Table S4, Supporting Information).[49–52] The superior performance was primarily due to the absence of an insulating binder in the coating process, which otherwise introduces inactive "dead mass". This dead mass not only fails to participate in charge storage but may also impede the transport of electrolyte ions, thereby diminishing the overall device performance.

To elucidate the performance advantages of MOF **2**, we conducted proton conductivity tests.[53,54] Electrochemical impedance spectroscopy measurements revealed that MOF **1** and MOF **2** exhibit high intrinsic conductivity with values of 6.41 × 10^{-3} and 6.53 × 10^{-2} S cm^{-1}, respectively, under conditions of 85 °C and 98% RH (**Figure 3**c,d). These values outperform the conductivity observed in the majority of bismuth-containing MOFs (Table S5, Supporting Information). The activation energies for proton transfer in MOF **1** and MOF **2** were calculated
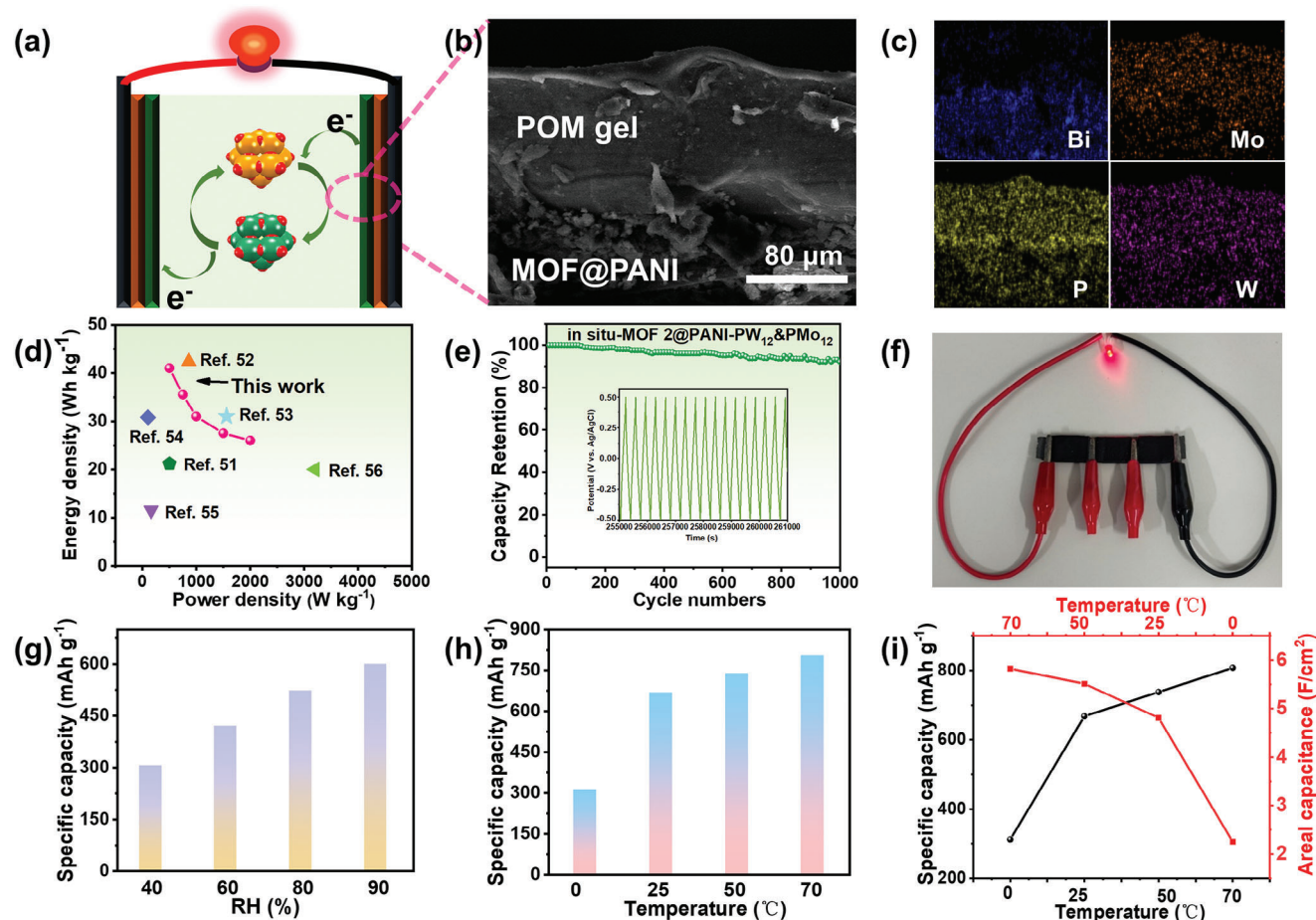
ADVANCED
SCIENCE NEWS

www.advancedsciencenews.com

ADVANCED
FUNCTIONAL
MATERIALS

www.afm-journal.de

Figure 3. a) Water uptake isotherms of MOF **1** and MOF **2**. b) Arrhenius plot for MOF **1** and MOF **2** (with least-squares fitting). Nyquist plots of c) MOF **1** and d) MOF **2** at 98% RH in the temperature range of 35–85 °C. e) Plausible conduction mechanism.

from Arrhenius plots to be 0.413 and 0.356 eV, respectively. Notably, the activation energy for proton transfer in MOF **2** was less than 0.4 eV, indicating that the proton conduction mechanism in MOF **2** follows the Grotthuss mechanism, involving proton hopping within abundant hydrogen-bonded networks (Figure 3e). This mechanism in MOF **2** enables swift proton delivery to the redox-active sites that are deeply embedded within the stacked frameworks. This attribute facilitates swift reaction kinetics and an elevated utilization rate of active sites, thereby yielding elevated power density and energy density.[55]

To explore the potential of the prepared supercapacitors for practical applications, we developed a capacitor system utilizing POMs electrolytes as both proton conductors and redox mediators. The system features two in situ-MOF n@PANI electrodes layered around the POM-gel electrolyte to enhance overall capacitance. The solid-state SCs, including in situ-MOF n@PANI-PW$_{12}$, in situ-MOF n@PANI-PMo$_{12}$, and in situ-MOF n@PANI-

PW$_{12}$&PMo$_{12}$, were assembled by clamping two sheets of in situ-MOF n@PANI electrodes to either side of the POM-gel electrolyte and then subjected to a hot-pressing treatment at 50 °C for 10 min (**Figure 4**a). Figure 4b presents a SEM image depicting the electrode-electrolyte interface. Figure 4c shows the elemental analysis mapping. It was concluded that P, W, and Mo atoms were dispersed uniformly in the electrolytes, the electrode-electrolyte interface, as well as the electrodes. For comparison, a control SC (H$_2$SO$_4$ SC) was also assembled using a sulfuric acid-gel electrolyte following the same procedure. The CV curves and GCD curves for in situ-MOF 1@PANI-H$_2$SO$_4$, -PW$_{12}$, -PMo$_{12}$, and -PW$_{12}$&PMo$_{12}$, as well as for in situ-MOF 2@PANI-H$_2$SO$_4$, -PW$_{12}$, -PMo$_{12}$, and -PW$_{12}$&PMo$_{12}$, were recorded at scan rates ranging from 20 to 300 mV s^{-1} (Figures S14–S21, Supporting Information). In situ-MOF n@PANI-PW$_{12}$ SCs exhibited similar electrochemical performance to the in situ-MOF n@PANI-H$_2$SO$_4$ SCs. In the PW$_{12}$-gel SCs, PW$_{12}$ functioned solely as a

ADVANCED
SCIENCE NEWS

www.advancedsciencenews.com

ADVANCED
FUNCTIONAL
MATERIALS

www.afm-journal.de

Figure 4. a) Schematic illustration of the assembled structure of in situ-MOF **2**@PANI-PW$_{12}$&PMo$_{12}$ SC. b) SEM image of electrode-electrolyte interface. c) Elemental analysis mapping of in situ-MOF **2**@PANI-PW$_{12}$&PMo$_{12}$ SC. d) Ragone plot of the as-synthesized device. e) Capacitance retention after 1000 cycles. f) A red LED illuminated by three devices in series. g) The specific capacity at different relative humidities. h) The specific capacity at different temperatures. i) Variation of C$_s$ and C$_a$ with different temperatures.

proton conductor, without contributing any redox activity. This contrasts with the PMo$_{12}$ SCs, which exhibited distinct redox peaks in CV curves. These peaks were complemented by corresponding plateaus in GCD curves, indicating a significant redox contribution from PMo$_{12}$. At a current density of 1 A g^{-1}, the PMo$_{12}$ SCs achieved a specific capacity of up to 249.72 mA h g^{-1} for MOF 1 and 263.89 mA h g^{-1} for MOF 2 significantly higher than those of PW$_{12}$ SCs (145.55 mA h g^{-1} for MOF 1 and 200.37 mA h g^{-1} for MOF 2) and H$_2$SO$_4$ SCs (117.54 mA h g^{-1} for MOF 1 and 174.23 mA h g^{-1} for MOF 2). This indicates that PMo$_{12}$ not only conducted protons but also enhanced the capacitive performance. By combining the excellent proton conductivity of PW$_{12}$ with the outstanding redox activity of PMo$_{12}$, the PW$_{12}$&PMo$_{12}$ SCs achieved a synergistic performance enhancement. As depicted in Figures S17 and S21 (Supporting Information), the mixed gel SC demonstrated superior electrochemical performance, with the highest specific capacity of 265.55 mA h g^{-1} and energy density of 13.27 Wh kg^{-1} for MOF 1, 366.94 mA h g^{-1} and 18.35 Wh kg^{-1} for MOF 2 outperforming many existing SCs (Figure 4d).[56–61] Additionally, the PW$_{12}$&PMo$_{12}$ SCs maintained an impressive capacitance retention of 92.6% after 1000 cycles (Figure 4e), which is also su-

perior to many existing supercapacitors in the field (Table S7, Supporting Information). It is validated that the functionality of PW$_{12}$ and PMo$_{12}$ within the hybrid gel capacitor was effectively enhanced by their respective contributions to each other. This research highlights the promise of POMs as potent electrolytes for SCs. Additionally, Figure 4f demonstrates the capability of three MOF **2**@PANI-PW$_{12}$&PMo$_{12}$ SCs in series to power a commercial LED, illustrating the material's potential in energy storage.

Due to its porous structure, in situ-MOF **2**@PANI exhibited excellent moisture absorption characteristics. Additionally, POMs possessed a certain degree of moisture absorption capacity. We anticipated that the assembled in situ-MOF **2**@PANI-PW$_{12}$&PMo$_{12}$ SC would effectively capture moisture from the surrounding environment and convert it into electricity. To explore the potential applications of MOF-based solid-state capacitors under a wider range of climatic conditions, we systematically assessed the electrochemical performance of MOF **2**@PANI-PW$_{12}$&PMo$_{12}$ composite supercapacitors in simulated atmospheric environments with fluctuating humidity and temperature. In the initial phase, we focused on the electrochemical behavior of the devices at four predetermined RH levels:

40%, 60%, 80%, and 90%. The experimental data revealed that the electrochemical performance of the capacitors significantly improves with the increase in environmental humidity (Figure S23, Supporting Information). Notably, at 90% RH, the supercapacitor exhibited an outstanding specific capacity of up to 619.44 mA h g^{-1}. Keeping the humidity constant (90% RH), we further investigated the electrochemical processes and stability of the capacitors by varying the environmental temperature. Notably, when the temperature is raised to 70 °C, the specific capacity value increases significantly, reaching 808.91 mA h g^{-1} (Figure S24, Supporting Information). The experimental results indicate that the supercapacitor demonstrates stable electrochemical performance across a wide temperature range from 0 to 70 °C, although it may not achieve peak performance levels at the extreme ends of this range. After 1000 cycles, the capacitance retention rates at these extreme temperatures were 80.71% and 87.02% (Figure S25, Supporting Information), respectively. However, at 80 °C, there was a marked decrease in charge and discharge time, which is attributed to the high temperature leading to the evaporation of water from the electrolyte, causing it to dry out and crack (Figure S26, Supporting Information). Such outstanding performance lays a solid scientific foundation for the scalable application of MOF-based supercapacitors under extreme climate conditions. The cycle stability was essential for a material to be considered viable for practical applications. Consequently, when exposed to alternating humidity conditions between 40% RH and 90% RH, the supercapacitor showed no significant decrease in specific capacitance even after three repeat cycles (Figure S27a, Supporting Information). However, when subjected to fluctuating temperatures between 0 and 70 °C, a slight decline in performance was observed (Figure S27b, Supporting Information). Despite this, the material's morphology remained unaltered after three complete temperature cycles (Figure S28, Supporting Information). Remarkably, even after three such cycles, the assembled solid-state supercapacitor was still able to power an LED bulb without any noticeable dimming (Figure S29, Supporting Information). This robust functionality further validates the device's usability and durability in practical applications.

3. Conclusion

In conclusion, this study successfully demonstrates the feasibility of integrating humidity harvest with energy storage in a solid-state supercapacitor system. By utilizing moisture-absorbent MOFs grown in situ on carbon paper electrodes and humidity-sensitive POMs as electrolytes, we have created a novel energy storage device that efficiently converts ambient humidity into electrical energy. The high energy density and excellent cycling stability of the constructed supercapacitor highlight its potential for practical applications in various environmental conditions. This research not only advances the field of humidity energy harvesting and storage but also opens up new avenues for the development of environmentally adaptive, high-performance energy storage technologies. Furthermore, the findings underscore the importance of material design strategies that harness the synergistic effects of electrode-electrolyte interfaces, paving the way for future innovations in renewable energy conversion and storage systems.

4. Experimental Section

The Experimental Section is available in the Supporting Information.

Supporting Information

Supporting Information is available from the Wiley Online Library or from the author.

Conflict of Interest

The authors declare no conflict of interest.

Data Availability Statement

Research data are not shared.

[1] X. Liu, H. Gao, J. E. Ward, X. Liu, B. Yin, T. Fu, J. Chen, D. R. Lovley, J. Yao, *Nature* **2020**, *578*, 550.
[2] T. Ji, W. Chen, Z. Kang, L. Zhang, *Nano Res.* **2023**, *17*, 1875.
[3] D. Maity, M. Fussenegger, *Adv. Sci.* **2023**, *10*, 2300750.
[4] Y. Liu, Z. Li, X. Yang, Y. Yang, X. Li, Y. Jiang, Y. Gao, L. Wang, W. Lü, *Adv. Funct. Mater.* **2024**, *34*, 2407204.
[5] B. Li, X. Duan, D. Cheng, X. Chen, Z. Gao, W. Ren, K.-Z. Shao, H.-Y. Zang, *J. Am. Chem. Soc.* **2023**, *145*, 2243.
[6] H. Yan, Z. Liu, R. Qi, *Nano Energy* **2022**, *101*, 107591.
[7] Z. Li, J. Wang, L. Dai, X. Sun, M. An, C. Duan, J. Li, Y. Ni, *ACS Appl. Mater. Interfaces* **2020**, *12*, 55205.
[8] G. Ren, Q. Hu, J. Ye, X. Liu, S. Zhou, Z. He, *Chem. Eng. J.* **2022**, *441*, 135921.
[9] H. Zhong, S. Wang, Z. Wang, J. Jiang, *Chem. Eng. J.* **2024**, *486*, 150203.
[10] K. Fan, X. Liu, Y. Liu, Y. Li, X. Liu, W. Feng, X. Wang, *Nano Energy* **2022**, *91*, 106605.
[11] L. Wang, H. Wang, C. Wu, J. Bai, T. He, Y. Li, H. Cheng, L. Qu, *Nat. Commun.* **2024**, *15*, 4929.
[12] N. Wang, Y. Zheng, Y. Feng, F. Zhou, D. Wang, *Nano Energy* **2020**, *77*, 105088.
[13] S. Li, W. Wu, X. Yan, *Renewables* **2023**, *1*, 142.
[14] Z. Lv, W. Li, J. Wei, F. Ho, J. Cao, X. Chen, *CCS Chem* **2023**, *5*, 11.

[15] Y. Wang, Y. Cui, D. Kong, X. Wang, W. Feng, P. Liu, T. Cai, X. Li, L. Zhao, D. Kong, L. Zhi, Q. Xue, Z. Yan, W. Xing, *Renewables* **2023**, *1*, 239.

[16] J. Yu, D. Qu, X. Wang, J. Ma, Y. Zheng, P. Zhang, X. Zhao, Y. Wang, P. Li, J. Zhang, *Adv. Funct. Mater.* **2024**, https://doi.org/10.1002/adfm.202414934.

[17] L. Zhao, Y. Li, J. Zhao, H. Zhang, P. Yuan, R. Song, *Adv. Funct. Mater.* **2024**, https://doi.org/10.1002/adfm.202413198.

[18] Z. Lu, X. Wang, H. Zong, D. Lan, Y. Sun, K. Zhao, B. Wang, J. Liu, *Chem. Eng. J.* **2024**, *157183*, 1385.

[19] T. Kang, P. Nakhanivej, K. J. Wang, Y. Chen, Y. G. Chung, H. S. Park, *J. Energy Chem.* **2024**, *94*, 646.

[20] J. Yesuraj, J. Kim, R. Yang, K. Kim, *Adv. Compos. Hybrid Mater.* **2024**, *7*, 69.

[21] N. R. Nadar, R. M. Rego, G. D. Kumar, H. J. Rao, R. K. Pai, M. D. Kurkuri, *J. Energy Storage* **2023**, *72*, 108670.

[22] J. Ding, Y. Yang, J. Poisson, Y. He, H. Zhang, Y. Zhang, S. Bao, S. Chen, Y.-M. Chen, K. Zhang, *ACS Energy Lett.* **2024**, *9*, 1803.

[23] D. Hu, Y. Jia, S. Yang, C. Lin, F. Huang, R. Wu, S. Guo, K. Xie, P. Du, *Chem. Eng. J.* **2024**, *488*, 151160.

[24] N. Devi, S. S. Ray, *Mater. Today Commun.* **2020**, *25*, 101691.

[25] S. Wu, D. Cai, Z. Tian, L. Guo, Y. Wang, *J. Energy Storage* **2024**, *89*, 111670.

[26] P.-P. Sun, Y.-H. Zhang, H. Shi, F.-N. Shi, *Chem. Eng. J.* **2022**, *427*, 130836.

[27] R. Vanaraj, S. Daniel, G. Mayakrishnan, K. Govindarasu Gunasekaran, B. Arumugam, C. M. Babu, S. C. Kim, *J. Colloid Interface Sci.* **2024**, *666*, 380.

[28] H.-B. Luo, Q. Ren, P. Wang, J. Zhang, L. Wang, X.-M. Ren, *ACS Appl. Mater. Interfaces* **2019**, *11*, 9164.

[29] M. I. Bashir, F. Anjum, M. Imran, H. M. Fahad, F. Sher, *J. Mater. Sci.: Mater. Electron.* **2024**, *35*, 742.

[30] C. Wang, Y. Wang, P. Cheng, L. Xu, F. Dang, T. Wang, Z. Lei, *Sens. Actuators, B.* **2021**, *340*, 129926.

[31] J. Lu, J. Li, J. Wan, X. Han, P. Ji, S. Luo, M. Gu, D. Wei, C. Hu, *Nano Res.* **2020**, *14*, 2410.

[32] A. D. Savariraj, C. Justin Raj, A. M. Kale, B. C. Kim, *Small* **2023**, *19*, 2207713.

[33] K. A. Milakin, D. V. Tumacder, O. Taboubi, U. Acharya, J. Hromádková, M. Lhotka, O. P. Georgievski, P. Bober, *ACS Appl. Energy Mater.* **2024**, *7*, 3354.

[34] Y. Wang, Y. Ding, X. Guo, G. Yu, *Nano Res.* **2019**, *12*, 1978.

[35] C. Wang, Z.-X. Gao, H.-Y. Zang, T.-W. Dong, Z.-M. Su, *Inorg. Chem. Front.* **2023**, *10*, 3641.

[36] B. Mahnoush, S. A. Rashid, S. Shafie, A. R. Sadrolhosseini, H. N. Lim, *Polymers* **2021**, *13*, 2003.

[37] Z. Duan, M. Zhang, L. Cui, H. Yu, K. Deng, Y. Xu, Z. Wang, L. Wang, H. Wang, *J. Mater. Chem. A* **2022**, *10*, 14435.

[38] J. Noh, S. Jekal, C. M. Yoon, *Adv. Sci.* **2023**, *10*, 2301923.

[39] X. Chen, C.-C. Zhao, J. Ren, B. Li, Q. Liu, W. Li, F. Yang, S. Lu, Y. Zhao, L.-K. Yan, H.-Y. Zang, *Chin. J. Catal.* **2024**, *62*, 209.

[40] Q. Liu, Y. Cui, L. Zhu, D. Cheng, C. Wang, S. Lu, B. Li, X. Chen, H.-Y. Zang, *Polyoxometalates* **2023**, *2*, 9140036.

[41] D. Cheng, K. Li, H.-Y. Zang, J.-J. Chen, *Energy Environ. Mater.* **2023**, *6*, e12341.

[42] W.-B. Ren, S. Sun, Z. Gao, B. Li, X. Chen, Q. Liu, H.-Y. Zang, *Inorg. Chem.* **2023**, *62*, 20506.

[43] H. Khan, J. Yang, M. Wang, J. Sun, H. Zhang, L. Yang, *Chem. Eng. J.* **2024**, *499*, 156129.

[44] B. Mandal, S. Saha, D. Das, J. Panda, S. Das, R. Sarkar, B. Tudu, *FlatChem* **2022**, *34*, 100400.

[45] J. Zhu, S. He, H. Tian, Y. Hu, C. Xin, X. Xie, L. Zhang, J. Gao, S. M. Hao, W. Zhou, L. Zhang, *Adv. Funct. Mater.* **2023**, *33*, 2301165.

[46] Z.-X. You, Y. Xiao, Q.-L. Guan, Y.-H. Xing, F.-Y. Bai, F. Xu, *Inorg. Chem.* **2022**, *61*, 13893.

[47] X. Hang, Y. Xue, Y. Cheng, M. Du, L. Du, H. Pang, *Inorg. Chem.* **2021**, *60*, 13168.

[48] R. Deka, R. Rajak, V. Kumar, S. M. Mobin, *Inorg. Chem.* **2023**, *62*, 3084.

[49] J. Pokharel, A. Gurung, A. Baniya, W. He, K. Chen, R. Pathak, B. S. Lamsal, N. Ghimire, Y. Zhou, *Electrochim. Acta* **2021**, *394*, 139058.

[50] G. Liu, S. Li, R. Baikeri, G. Wang, Z. Jin, *J. Electroanal. Chem.* **2023**, *945*, 117674.

[51] M. Safari, J. Mazloom, *J. Solid State Electrochem.* **2021**, *25*, 2189.

[52] S. Ghosh, C. K. Maity, G. C. Nayak, H. P. Nayek, *J. Solid State Chem.* **2020**, *282*, 121093.

[53] N. Ma, S. Impeng, S. Bureekaew, N. Morozumi, M. Haga, S. Horike, *J. Am. Chem. Soc.* **2023**, *10*, 9808.

[54] S. C. Pal, D. Mukherjee, Y. Oruganti, B. G. Lee, D.-W. Lim, B. Pramanik, A. K. Manna, M. C. Das, *J. Am. Chem. Soc.* **2024**, *146*, 14546.

[55] Y. Yang, P. Zhang, L. Hao, P. Cheng, Y. Chen, Z. Zhang, *Angew. Chem., Int. Ed.* **2021**, *60*, 21838.

[56] A. Narayanan, A. Siddiqa, N. K. Kodihalli, G. Hegde, D. H. Nagaraju, M. Padaki, *ACS Sustain. Chem. Eng.* **2023**, *11*, 3750.

[57] G. Xiao, J. Fan, H. Liao, S. Gao, S. Li, K. Cui, W.-B. Luo, C.-Q. Niu, Z.-S. Chao, *Energy Fuels* **2022**, *36*, 5928.

[58] N. Ahmad, A. Rinaldi, M. Sidoli, G. Magnani, A. Morenghi, S. Scaravonati, V. Vezzoni, L. Pasetti, L. Fornasini, F. Ridi, C. Milanese, M. Riccò, D. Pontiroli, *J. Power Sources* **2024**, *99*, 113267.

[59] Q. Liu, M. Yang, Y. Deng, M. Zhang, C. Liu, F. Hu, X. Jian, Y. Chen, *J. Power Sources* **2024**, *602*, 234336.

[60] Q. Zheng, X. Li, Q. Yang, C. Li, G. Liu, Y. Wang, P. Sun, H. Tian, C. Wang, X. Chen, J. Shao, *J. Power Sources* **2022**, *524*, 231102.

[61] M. Thomas, S. Veleva, B. Karamanova, A. Brigandì, N. Rey-Raap, A. Arenillas, A. Stoyanova, F. Lufrano, *Sustain. Mater. Technol.* **2023**, *38*, e00770.